

# Gate tunable Dirac mass and Berry phase in Trilayer graphene

Harsimran Kaur Mann<sup>1†</sup>, Simrandeep Kaur<sup>1†</sup>, Safil Mullick<sup>1</sup>, Priya  
Tiwari<sup>2</sup>, Kenji Watanabe<sup>3</sup>, Takashi Taniguchi<sup>4</sup>, Aveek Bid<sup>1\*</sup>

<sup>1</sup>*Department of Physics, Indian Institute of Science, Bangalore 560012, India*

<sup>2</sup>*Braun Center for Submicron Research,*

*Department of Condensed Matter Physics,*

*Weizmann Institute of Science, Rehovot, Israel*

<sup>3</sup>*Research Center for Electronic and Optical Materials,*

*National Institute for Materials Science,*

*1-1 Namiki, Tsukuba 305-0044, Japan*

<sup>4</sup>*Research Center for Materials Nanoarchitectonics,*

*National Institute for Materials Science,*

*1-1 Namiki, Tsukuba 305-0044, Japan*

<sup>†</sup> *These authors contributed equally*

*\*email: aveek@iisc.ac.in*

## Abstract

In-situ control over band mass inversion is crucial for developing materials with topologically protected edge modes. In this Letter, we report the direct observation of displacement field  $D$  control of band mass and Berry phase in Bernal stacked trilayer graphene (TLG) in the region where trigonal warping distorts the quadratic band into off-center Dirac points, referred to as ‘Dirac Gullies.’ Using Shubnikov-de-Haas (SdH) oscillations, we map the Fermi surface contours of the Dirac gullies and the  $D$ -dependent band structure. With increasing  $D$ -field, the Berry phase undergoes multiple transitions from  $\Phi_B = 2\pi \rightarrow \pi \rightarrow 2\pi$  as  $D$  is varied. Concurrently, measurement of the effective mass reveals a series of transitions between massless and massive bands, signaling the closure and reopening (accompanied by a possible band inversion) of the band gap at a critical value of  $D$ . Interestingly, the expected Dirac-like behavior of the Dirac gullies ( $\Phi_B = \pi$ ) persists only over a narrow range of  $D$ . Our study directly confirms recent predictions of  $D$ -field-induced band inversion in the low-energy regions of TLG. It is a significant step towards achieving control over pure valley transport in multilayer graphene.

*Introduction:*—The concept of the Berry phase  $\Phi_B$  [1] pervades virtually every branch of modern quantum condensed matter physics, driving a diverse range of quantum phenomena, including orbital magnetization, electric polarization, and anomalous transport effects [2–4]. It is a powerful theoretical tool, allowing physicists to link geometric considerations in quantum wave functions to tangible, measurable properties of materials [5–10]. It is also closely related to topological invariants, such as the Chern number or  $Z_2$  invariant, which characterize topological phases such as topological insulators, Weyl semi-metals, and other exotic quantum phases [11, 12]. Several of these topologically non-trivial phases originate from band inversion [13–17]. The ability to manipulate both the Berry phase and band inversion is essential for discovering new materials with robust, topologically protected surface or edge states resistant to disorder and backscattering.

Recently, the study of the Berry phase in multilayer graphene systems, particularly at low charge carrier densities, has garnered significant interest. This surge is driven by the understanding that the low-energy bands of these systems are trigonally warped into sets of  $C_3$ -symmetric, off-center offshoots with linear dispersion, called ‘Dirac Gullies’ [18–24]. This band distortion leads to novel correlated phases [25, 26], interaction-driven nematic phases [21, 27] and multiple Lifshitz transitions [18, 28, 29]. The band topology of these Gullies is predicted to be Dirac-like with expected Berry phase of  $\pi$  for each gully [5, 22]. Moreover, the effective band mass  $m^*$  and

the strength of these Dirac-like features can be tuned by an external displacement field  $D$  [20–22]. However, experimental realizations of these properties remain elusive.

In this Letter, we investigate the band structure topology of the Dirac gully in ultra-high quality Bernal stacked trilayer graphene (TLG). We map out the Fermi surface of the gullies using Shubnikov de Haas (SdH) oscillations [30] and probe the evolution of the  $\Phi_B$  and  $m^*$  with  $D$ . Our study reveals a strong  $D$ -tunability of  $\Phi_B$  and  $m^*$ . Specifically, at low  $D$ , the gullies are massive with a relatively large  $m^*$ , and  $\Phi_B = 2\pi$ . As  $D$  increases, the gullies deepen, and  $m^*$  decreases sharply, accompanied by a transition of  $\Phi_B$  to  $\pi$ , signifying a transition to massless Dirac gullies. Intriguingly, at still higher  $D$ , the effective mass  $m^*$  increases again with  $\Phi_B$  reverting to  $2\pi$ . Our study establishes the band characteristics of the low-energy chiral quasiparticles in trilayer graphene as strongly displacement field tunable, with expected Dirac-like behavior ( $\Phi_B = \pi$ ) persisting only over a specific range of  $D$ .

*Quantum oscillations*:- The measurements were performed on a high-mobility hexagonal boron nitride (hBN) encapsulated TLG device with a top and back graphite gates (Supplementary Information, section S1)[31]. The dual graphite gate configuration is used for simultaneous tuning of the perpendicular displacement field  $D = [(C_{bg}V_{bg} - C_{tg}V_{tg})/2\epsilon_0 + D_0]$  and number density  $n = [(C_{bg}V_{bg} + C_{tg}V_{tg})/e + n_0]$  independently. Here  $C_{bg}$  ( $C_{tg}$ ) is the back-gate (top-gate) capacitance, and  $V_{bg}$  ( $V_{tg}$ ) is the back-gate (top-gate) voltage.  $D_0$  and  $n_0$  are the graphene's residual displacement field and number density due to impurities. All the measurements were performed using standard low-frequency lock-in detection techniques in a dilution refrigerator with a base temperature of 20 mK.

Bernal-stacked trilayer graphene (hereafter referred to as TLG) is a multi-band system formed by monolayer-like (MLL) linear bands and bilayer-like (BLL) quadratic bands (Fig. 1(a)) at zero interlayer potential ( $\Delta = 0$  meV). These two bands are protected by mirror symmetry from intermixing. Applying a displacement field  $D$  perpendicular to the interface breaks the mirror symmetry and hybridizes the MLL and the BLL bands. In the presence of a finite  $D$ , the MLL band splits into three sections:  $M1$ ,  $M2$ , and  $M3$ , as shown in the right panel of Fig. 1(a). With increasing  $D$ , the MLL bands  $M1$  and  $M3$  shift to higher energies. Importantly, for our purposes, the  $M2$  band merges with the BLL band and develops into a novel set of  $C_3$ -symmetric Dirac gullies.

The measured SdH oscillations at  $n = -2.52 \times 10^{16} \text{ m}^{-2}$  at  $D = 0 \text{ V/nm}$  are presented Fig. 1(b); the data are taken along the black dotted line in Fig. 1(a). The beating pattern in the oscillations arises from the coexistence of two distinct Fermi surface areas. Recall that at fixed chemical

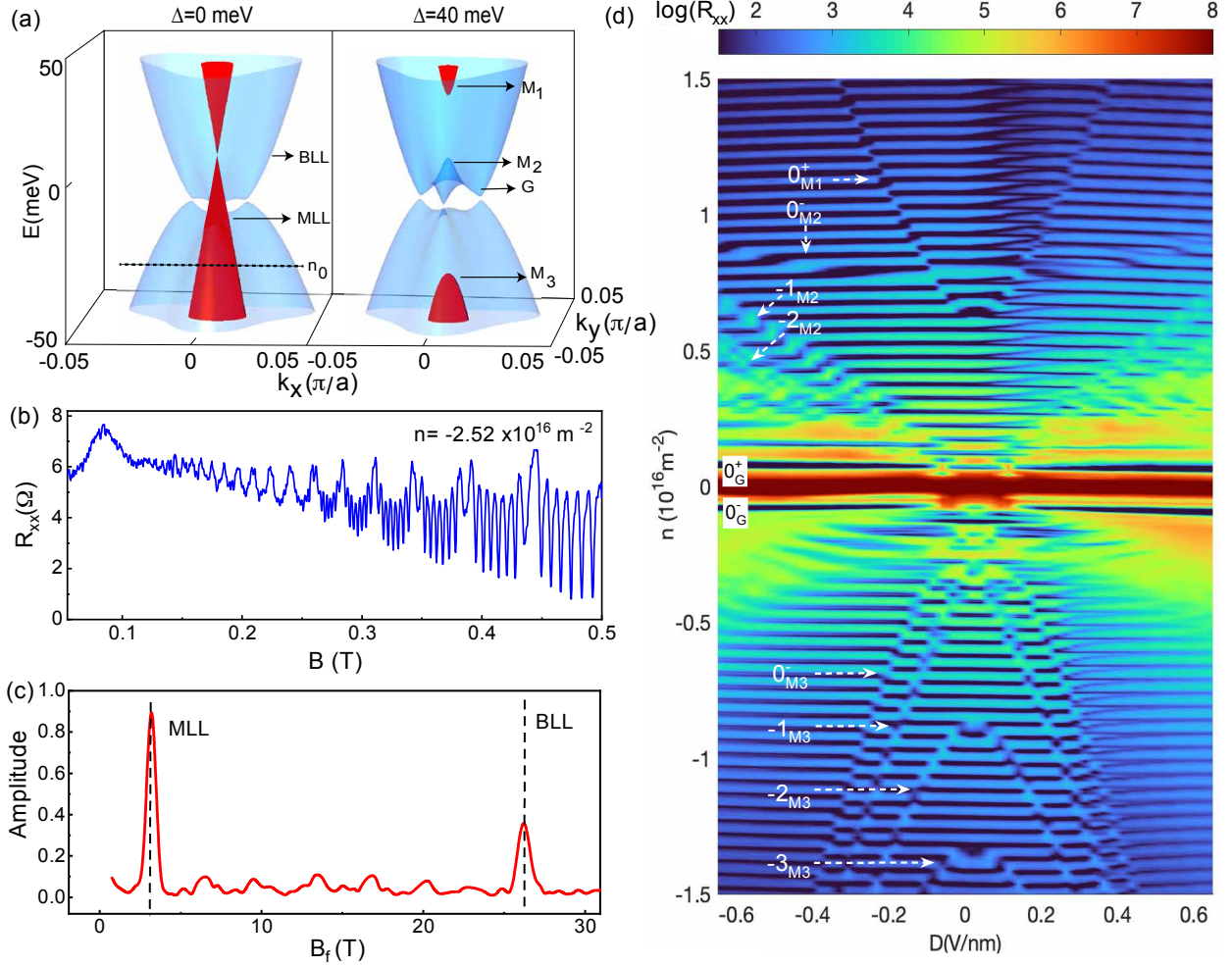


FIG. 1. **Device Characterization:** (a) Calculated band structure for ABA TLG at  $\Delta = 0$  meV and  $\Delta = 40$  meV.  $a = 2.46 \times 10^{-10} \text{ m}^{-2}$  is carbon-carbon distance. (b) SdH oscillations measured at  $n = -2.52 \times 10^{16} \text{ m}^{-2}$  and  $T = 20$  mK showing beating pattern with two frequencies. (c) Fast-Fourier Transform (FFT) of (b) showing two primary frequencies of MLL and BLL bands. (d) Contour plot of  $R_{xx}$  versus  $n$  and  $D$  in a log-scale. The data were measured at  $T = 20$  mK and  $B = 0.5$  T. The labels in the plot refer to the Landau levels.

potential (equivalently fixed  $n$ ), the amplitude of SdH oscillations  $\Delta R_{xx} \propto \cos[2\pi(B_f/B + \gamma)]$  with  $B_f = \hbar S / (2\pi e) = nh / (ge)$  and  $\gamma = (\Phi_B / 2\pi - 1/2)$  [32, 33]. Here,  $R_{xx}$  is the longitudinal resistance,  $S$  is the area enclosed by the Fermi contour,  $g$  is the degeneracy of Landau levels and  $\Phi_B$  is the Berry phase. The Fast Fourier transform (FFT) of oscillations shows two primary frequencies (Fig. 1(c)). The lower (higher) frequency corresponds to the MLL (BLL) band with a smaller (larger) Fermi contour area. By systematically tracking these frequencies at different  $n$  and  $D$ ,

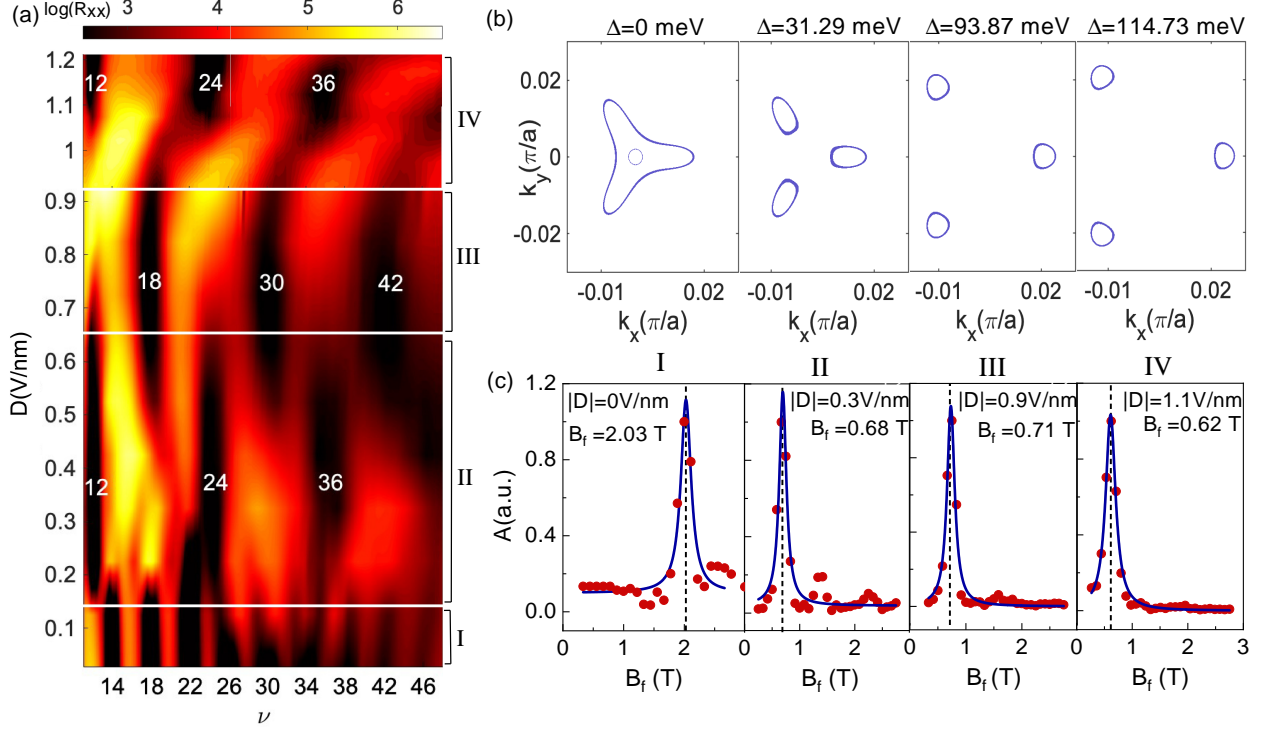


FIG. 2. **Dependence of  $\nu$  on  $D$**  : (a) Contour map of  $R_{xx}$  versus  $D$  and  $\nu$  measured at constant  $n = 1.8 \times 10^{15} \text{ m}^{-2}$  and  $T = 20 \text{ mK}$ . (b) Plots of Fermi contour and (c) FFT of SdH measured oscillations for representative values of  $D$  in region 1 ( $D = 0 \text{ V/nm}$ ), region 2 ( $|D| = 0.3 \text{ V/nm}$ ), region 3 ( $|D| = 0.9 \text{ V/nm}$ ) and region 4 ( $|D| = 1.1 \text{ V/nm}$ ).  $a = 2.46 \times 10^{-10} \text{ m}^{-2}$  is carbon-carbon distance.

we map out the complex band structure of ABA TLG and its evolution with  $D$  (Supplementary Information, section S2).

Fig. 1(d) is a contour plot of  $R_{xx}$  as a function of  $n$  and  $D$ , measured at  $B = 0.5 \text{ T}$ . The plot shows crossings between the Landau levels of the MLL band (labeled  $M1$ ,  $M2$ , and  $M3$ ) and the four-fold degenerate BLL bands. At finite  $D$  bands, the  $M2$  band emerges, and the  $M1$  and  $M3$  bands move to higher number densities. At high  $D$ , near the charge neutrality point, the  $C_3$ -symmetric Dirac gully regime (denoted as  $G$ ) emerges. These multiple Lifshitz transitions arising from the  $D$ -induced electronic band modification, previously detected only through highly sensitive quantum capacitance measurements[27] and de Haas-van Alphen quantum oscillations[28], were observed in our sample due to its high quality.

A contour plot of SdH oscillations as a function of filling factor  $\nu$  and  $D$  measured at  $n = 1.8 \times 10^{15} \text{ m}^{-2}$  is presented in Fig 2(a). We identify four distinct  $D$ -regions regions with unique Landau level sequences. For low displacement fields  $0 \leq D \leq 0.15 \text{ V/nm}$  (labeled **region 1**), the

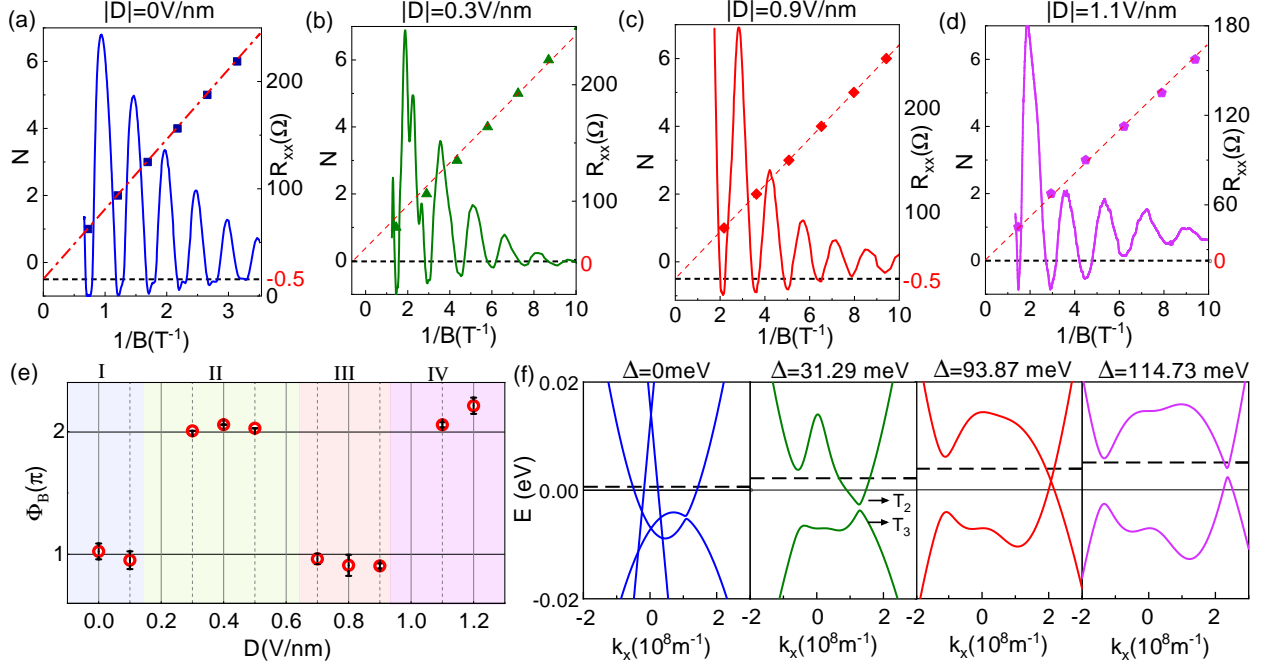


FIG. 3. **Calculation of Berry phase:** Plots of the Landau level index  $N$  (left axis) and  $R_{xx}$  (right axis) as a function of  $1/B$  for (a)  $D = 0$  V/nm (solid blue line), (b)  $D = 0.3$  V/nm (solid green line), (c)  $D = 0.9$  V/nm (solid red line), and (d)  $D = 1.1$  V/nm (solid violet line). The scatter plots show the Landau level index ( $N$ ) vs  $1/B$ . The dotted red lines fit the  $N$  versus  $1/B$  data. The y-intercepts of the lines give the Berry phase  $\Phi_B$ . (e)  $\Phi_B$  as a function of  $D$ . The Roman numerals on the top indicate the four distinct regimes of  $D$ . (f) Calculated band structure for four representative values of  $D$  in region 1 ( $D = 0$  V/nm), region 2 ( $|D| = 0.3$  V/nm), region 3 ( $|D| = 0.9$  V/nm) and region 4 ( $|D| = 1.1$  V/nm). The black dashed lines mark the position of the Fermi energy for  $n = 1.8 \times 10^{15}$  m<sup>-2</sup>.

$R_{xx}$  minima appear at  $\nu = 14, 18, 22, \dots$ , following the sequence  $\nu = 4(N_B + 1/2)$ , where  $N_B$  is the Landau level index of BLL (the factor  $1/2$  arises from the underlying zeroth Landau levels of MLL band [34]). As  $D$  increases, BLL bands deform into three different gullies. The prominent Landau levels in this region appear at  $\nu = 12, 24, 36$  in region 2 ( $0.15 \leq D \leq 0.65$  V/nm), changing the sequence abruptly to  $\nu = 12(N_G)$ , where  $N_G$  is the Landau level index of gullies. Interestingly, as we increase  $D$  to higher values (**region 3**,  $0.65$  V/nm  $\leq D \leq 0.9$  V/nm), we observe prominent minima at  $\nu = 18, 30, 42$ , changing the Landau level sequence to  $\nu = 12(N_G + 1/2)$ . At much higher  $D$ , Landau level sequence reverts to  $\nu = 12N_G$  (**region 4**,  $0.9$  V/nm  $\leq D \leq 1$  V/nm).

To understand this evolution of the Landau level sequence with  $D$ , we performed tight-binding calculations based on Slonczewski-Weiss-McClure model [35–37] with parameters from [21] to

calculate the band structure topology in the four different regions. Fig. 2(b) shows the resultant Fermi surface contours at different interlayer potential  $\Delta$ . At low  $D$ -fields (region-1), the perturbation to the pristine band structure is minimal, and one can still distinguish the MLL and BLL bands. We find two Fermi contours; the inner circular contour arises from the MLL band, while the outer trigonally warped contour is from the BLL band. Consequently, at low- $D$  and low- $n$ , one observes the characteristic  $4N_B + 2$  Landau level progression with  $4N_B$  Landau levels coming from the BLL band and the 2 additional Landau levels from the zeroth Landau level of the MLL band. The FFT spectrum of the SdH oscillations reveals a single frequency at 2.203 T (Fig. 2(c)), which corresponds to the BLL band; the frequency of the MLL band ( $B_f \leq 0.4$  T) is too small to be observed in low- $B$  SdH measurements.

As the  $D$  is increased to 0.3 V/nm, the Dirac Gullies emerge. We are now in region 2 where, at low energies, the single BLL band of  $D = 0$  is split into three disconnected Fermi pockets (Fig. 2(b)). Consequently, the Landau level degeneracy changes from 4 to 12 (each gully has 2-fold spin and 2-fold valley degeneracy). As the density of state remains almost unchanged, the area of each Fermi contour (and the corresponding  $B_f$ ) becomes one-third of its value in region 1 (recall that  $B_f \propto n/g$ ) – precisely what we observe in Fig. 2(c) for  $D = 0.3$  V/nm. In regions 3 and 4, the separation between the Gullies increases. Still, since  $n$  and the level degeneracy  $g$  are the same as in **region 2**, the area of each Fermi pocket and  $B_f$  remains virtually unchanged.

*Tuning the Berry phase with  $D$ :* To account for the abrupt changes in the Landau level sequence, we estimated the Berry phase in these four different regions. Fig. 3(a-d) show plots of  $R_{xx}$  (right axis) and the Landau level index  $N$  corresponding to minima in  $R_{xx}$  (left axis) as a function of  $1/B$  for representative values of  $D$  corresponding to the four regions (Supplementary Information, section S3). The y-axis intercept of the linear fit to the data (red dotted line in Fig. 3(a-d)) gives the Berry phase,  $\Phi_B$  in units of  $\pi$  (Supplementary Information, section S4). The evolution of  $\Phi_B$  with  $D$  is plotted in Fig. 3(e). In region 1,  $\Phi_B = \pi$ , this observation matches previous studies and is understood to originate from the underlying  $0_{M2^-}$  band that adds two additional Landau levels to the sequence of BLL bands [34]. In region 2,  $\Phi_B = 2\pi$  indicates that the gullies are massive in this region. With increasing  $D$  in region 3, the Berry phase jumps abruptly to  $\Phi_B = \pi$ , and the gullies turn massless. In region 4,  $\Phi_B$  changes back to  $2\pi$ , and the gullies become massive again. This  $D$ -field controlled mass inversion of the Dirac gullies is the central result of Letter.

The observed evolution of  $\Phi_B$  with  $D$  corroborates well with theoretical predictions [21]. Fig. 3(f) shows the calculated band structure at the four values of  $D$ ; the dotted line marks the

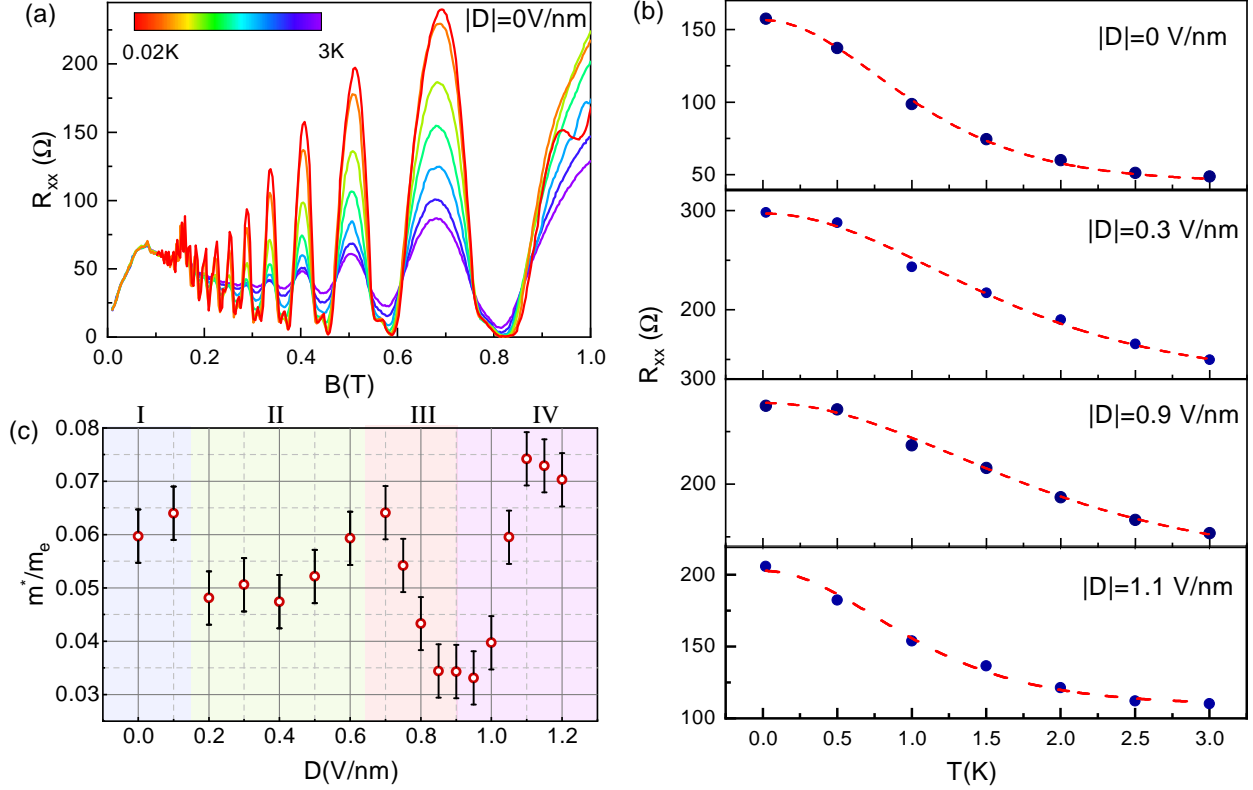


FIG. 4. **Calculation of effective mass:** Plots of the  $R_{xx}$  as a function of  $B$  measured for  $D = 0$  V/nm over the temperature range  $0.02K \leq T \leq 3K$ . (b) Plots of the amplitude of SdH oscillations as a function of  $T$  for  $D = 0$  V/nm,  $D = 0.3$  V/nm,  $D = 0.9$  V/nm, and  $D = 1.1$  V/nm. The red dotted lines fit the data points using the Lifshitz-Kosevich relation. (c) Plot of the effective mass  $m^*$  (scaled by the mass of free electron  $m$ ) as a function of  $D$  (red open circles). The error bars result from the scatter in the value of  $m^*$  when calculated from the different peaks in (a).

Fermi energy  $E_F$  corresponding to  $n = 1.8 \times 10^{15} \text{ m}^{-2}$ . At  $D = 0$  V/nm, the  $E_F$  lies in the valence band of the MLL sector; this results in the measured  $\Phi_B = \pi$ . For  $D = 0.3$  V/nm and  $D = 0.9$  V/nm the  $E_F$  lies in the  $T_2$  gully. However, there is a stark difference in the structure of the gully at these two displacement fields; while at  $D = 0.3$  V/nm, the gully is massive, it changes to massless at higher  $D$ . For higher  $D$ , the band gap between  $T_2$  and  $T_3$  gullies closes and reopens, resulting in the band becoming massive again for  $D \geq 0.9$  V/nm (Supplementary Information, section S5).

*Tuning the effective mass with  $D$ :*- To confirm the above assertion, we measured the effective mass of the Dirac Gully as a function of  $D$ . The effective mass of a band is directly proportional to the gap [22]. Representative plots of the temperature-dependent SdH oscillations at  $D = 0$  V/nm



measured over the temperature range 20 mK–3 K are plotted in Fig. 4(a). The effective mass  $m^*$  is extracted by fitting the maxima of the amplitude of the  $R_{xx}$  oscillations at a fixed  $B$  to the equation [32]:

$$\Delta R_{xx} \propto \frac{\lambda}{\sinh \lambda} \cos \left( 2\pi \left( \frac{B_f}{B} + \gamma \right) \right) \quad (1)$$

with the amplitude of oscillations,

$$\lambda = \frac{2\pi^2 k_B T m^*}{\hbar e B} \quad (2)$$

The dotted red lines in Fig. 4(b) show the fit to the  $R_{xx}$  maxima to Eqn. 1 at different values of  $D$  from the four different regions. Fig. 4(c) shows the extracted effective mass for the four regions (red open circles). For region 1, the  $m^* = 0.06 \pm 0.005m_e$  ( $m_e$ : mass of an electron) is very close to that of the BLL band. The effective mass changes to  $m^* \sim 0.05 \pm 0.005m_e$  in region 2. In this regime, the gullies are massive. With increasing  $D$ , the value of  $m^*$  passes through a sharp minimum at  $D_c = 0.9$  V/nm. The  $D$ -dependence of  $m^*$  tracks the massive  $\rightarrow$  massless  $\rightarrow$  massive topological phase transition of the Dirac gullies in conformity with the measured Berry phase. It is highly probable that beyond  $D_c$ , the bands invert; however, the current measurements are insensitive to this effect.

*Summary:-* Based on our measurements and analysis, we propose the following evolution of the low-energy trigonally warped region under a displacement field in Bernal-stacked trilayer graphene. At low  $D$ , the Dirac gullies are massive, exhibiting a Berry phase of  $\Phi_B = 2\pi$ . As  $D$  increases, the band mass decreases, and the gap between the  $T_2$  and  $T_3$  gullies closes beyond a critical displacement field of approximately  $D \sim 0.9$  V/nm. In this regime, the Berry phase shifts to  $\Phi_B = \pi$ , signaling the emergence of massless gullies. With further increase in  $D$ , the band gap reopens, leading to a reappearance of massive Dirac gullies (with  $\Phi_B = 2\pi$ ), now likely characterized by a negative band mass. These findings provide direct experimental validation of the theoretically predicted band mass inversion of the  $T_2$  and  $T_3$  gullies under an external displacement field [20–22].

The theory also anticipates the emergence of edge modes in this band-inverted regime, characterized by quantized single-valley Hall conductivity [22]. However, our measurements do not reveal these modes, likely due to the extremely small band gaps predicted within the experimentally accessible range of  $D$  (on the order of meV). As a result, the physics at the charge neutrality point is primarily influenced by impurity broadening. Investigating these predicted edge modes remains an open question for future studies using higher-quality devices.

## ACKNOWLEDGMENT

The authors acknowledge fruitful discussions with Tanmoy Das. A.B. acknowledges funding from the Department of Science & Technology FIST program and the U.S. Army DEVCOM Indo-Pacific (Project number: FA5209 22P0166). K.W. and T.T. acknowledge support from JSPS KAKENHI (Grant Numbers 19H05790, 20H00354, and 21H05233).

## Supporting Information

Supporting information contains detailed discussions of the (S1) Device fabrication, (S2) Probing  $D$ -dependence of band structure using SdH oscillations, (S3) Calculation of  $\nu$  from Landau Level Index  $N$ , (S4) Calculation of Berry Phase  $\Phi_B$  from SdH oscillations (S5) Evolution of  $T_2$  and  $T_3$  gullies with displacement field  $D$  and (S6) Evolution of Landau Level sequence and Berry phase with  $n$  and  $D$ .

## SUPPLEMENTARY INFORMATION

### S1. DEVICE FABRICATION

Trilayer graphene (TLG) and hexagonal boron nitride (hBN) flakes were mechanically exfoliated onto Si/SiO<sub>2</sub> substrates. The hBN flakes had a thickness of 25-30 nm. The TLG flakes were identified from optical contrast under a microscope and later confirmed using Raman spectroscopy [38, 39]. To make the stack, the flakes are picked up using polycarbonate film (PC film) in the sequential order of graphite/hBN/TLG/hBN/graphite. The stack is then transferred to Si/SiO<sub>2</sub> substrate along with PC film, followed by removing the PC residue in chloroform. The heterostructure is then annealed in a vacuum at 300°C for 4 hours. Electron beam lithography was used to define the contacts. This was followed by etching with a mixture of CHF<sub>3</sub> (40 sscm) and O<sub>2</sub> (10 sscm). The metallization was done with Cr/Pd/Au (3 nm/12 nm/55 nm) to form the 1-D contacts with TLG. Fig. S1(a) shows an optical image of the device. The graphene contacts are doped to higher number densities using SiO<sub>2</sub> gate to avoid p-n junction formation [31].

To calculate the mobility of the device the measured  $R_{xx}$  as a function of number density at  $D = 0V/nm$  and  $B = 0T$  is fit to the equation  $R = R_c + \frac{L}{W e \mu \sqrt{n^2 + n_0^2}}$  [40]. Here,  $R_c$ ,  $L$ ,  $W$ , and  $\mu$  are the contact resistance, length, width, and mobility of the device, respectively. From the fit (Fig. S1) (c), the extracted mobility is  $\mu = 62 \text{ m}^2\text{V}^{-1}\text{s}^{-1}$  and the intrinsic carrier concentration induced by charge impurity  $n_0 = 7.81 \times 10^{13} \text{ m}^{-2}$  reflecting the high quality and low impurity levels of the sample.

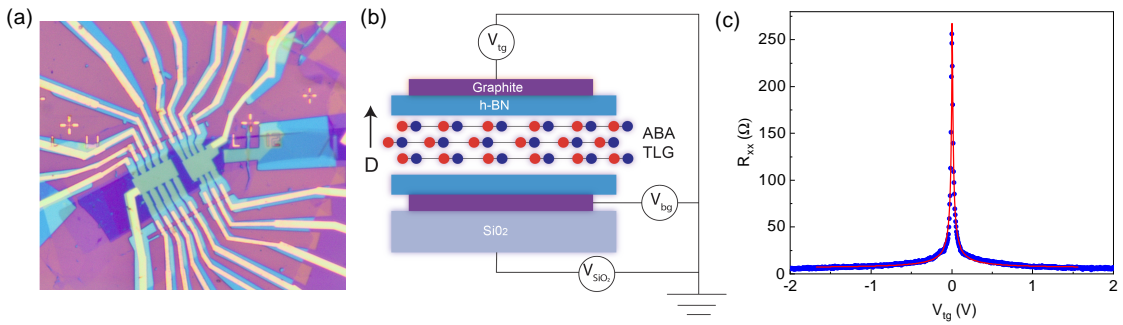


FIG. S1. **Device Characterization:**(a) Optical image of dual graphite gated TLG device. (b) Schematic of the device. (c) Measured  $R - V_g$  curve (blue circles). The fit (solid red curve) gives mobility  $\mu = 62 \text{ m}^2\text{V}^{-1}\text{s}^{-1}$  and the intrinsic carrier concentration induced by charge impurity  $n_0 = 7.81 \times 10^{13} \text{ m}^{-2}$ .

## S2. PROBING $D$ -DEPENDENCE OF BAND STRUCTURE USING SDH OSCILLATIONS

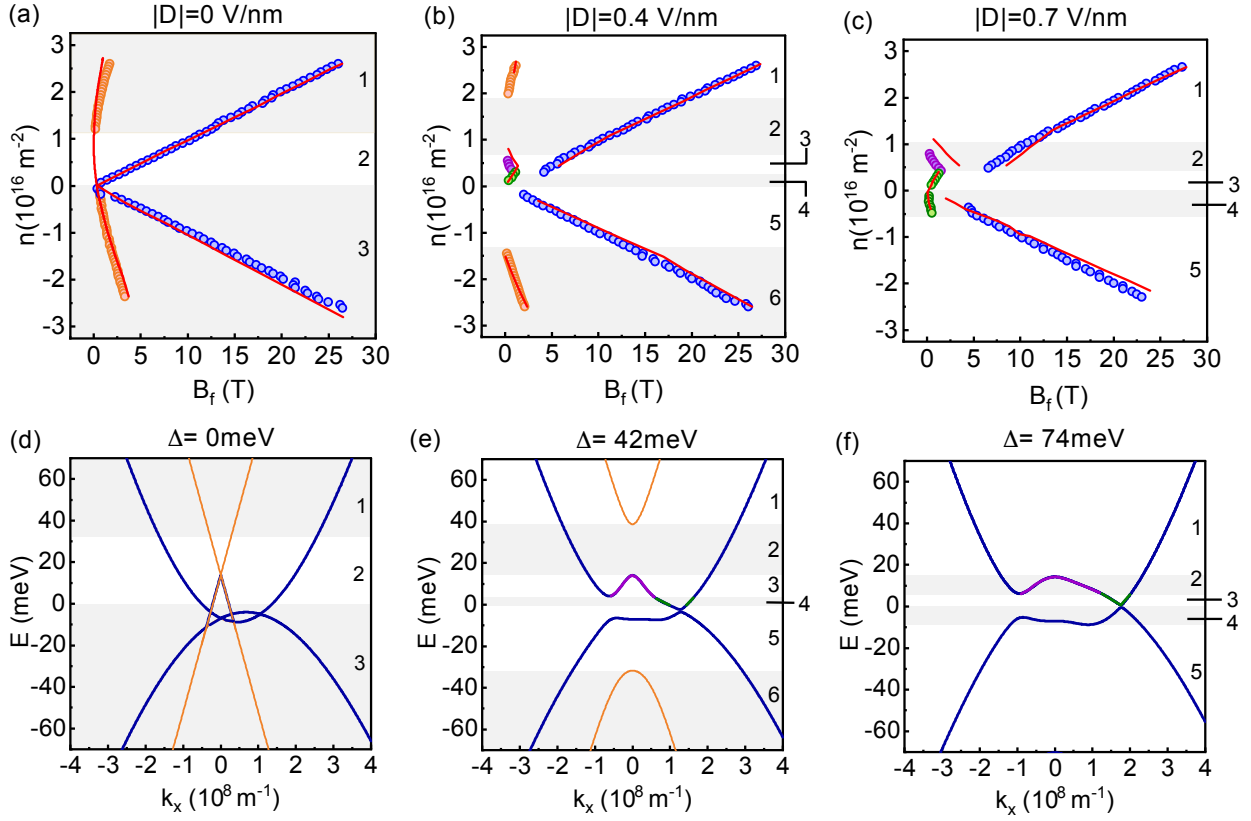


FIG. S2.  **$D$ -dependent band structure:** Number density  $n$  versus SdH frequency  $B_f$  obtained experimentally for constant  $D$  (a)  $|D| = 0 \text{ V/nm}$  (b)  $|D| = 0.4 \text{ V/nm}$  and (c)  $|D| = 0.7 \text{ V/nm}$ . The open circles show the experimentally obtained  $B_f$ ; Blue- BLL band, orange- MLL band  $M_1$  and  $M_3$ , violet- MLL band  $M_2$  and green- Gully. Red solid lines show the theoretically calculated  $B_f$  as function of  $n$  calculated from the  $E - k$  diagrams shown in (d)  $|D| = 0 \text{ V/nm}$  (e)  $|D| = 0.4 \text{ V/nm}$  and (f)  $|D| = 0.7 \text{ V/nm}$ . Regions 1 – 6 show the correspondence between the  $n - B_f$  and  $E - k$  plots.

We used Shubnikov de Haas oscillations (SdH) to map out the Fermi surfaces of the bands and study their evolution with  $D$ . For a fixed number density  $n$ , the SdH oscillation amplitude  $\Delta R_{xx} \propto \cos[2\pi(B_f/B + \gamma)]$  with the SdH frequency  $B_f = \hbar S / (2\pi e)$ . Here,  $R_{xx}$  is the longitudinal resistance,  $\gamma$  is the geometric phase, and  $S$  is the area enclosed by the Fermi contour. Fig. S2(a-c) shows  $B_f$  versus  $n$  plots measured at  $D = 0 \text{ V/nm}$ ,  $0.4 \text{ V/nm}$  and  $0.7 \text{ V/nm}$ , respectively. The calculated band structure at these values of displacement fields  $D$  is plotted in Fig. S2(d-f). The data acquired at  $D = 0 \text{ V/nm}$  can be divided into three distinct regions; these are marked in

Fig. S2(a) and (d). In regions 1 and 3, we identify the Monolayer-like (MLL) band (orange open circles) and the Bilayer-like(BLL) band (blue open circles). In region 2, near the Dirac point of the MLL band, the fermi surface area  $S$  (and consequently  $B_f$ ) becomes immeasurably small. We are thus left with only the value of  $B_f$  for the BLL band in this region.

At  $D = 0.4$  V/nm, the energy spectrum becomes markedly more complex as seen from Fig. S2(b) and Fig. S2(e). It is now convenient to divide the data into six distinct regions. As discussed in the introduction in the main paper, at a finite- $D$ , the MLL band is split into three parts; we identify all three segments of the MLL band from our data along with the Dirac gullies. In region 1, we find  $M_1$  (open orange circles) and the BLL (open blue circles) bands. Region 2 lies in the gap of the MLL band (Fig. S2(e)); this explains the appearance of only a single  $B_f$  in this range of number density (energy) originating from the BLL band (Fig. S2(b)). Region 3 hosts the  $M_2$  section of the MLL band (open violet circles in Fig. S2(b)) and the tail of the BLL band (open blue circles in Fig. S2(b)). At very low number densities (region 4), the Dirac gullies emerge (Fig. S2(e)) – their oscillation frequencies are plotted as open green circles in Fig. S2(b). On the hole side, region 5 contains only the BLL band while region 6 has both the  $M_3$  (open orange circles) and the BLL (open blue circles) bands.

Similar features are observed for  $D = 0.7$  V/nm (Fig. S2(c) and Fig. S2(f)). At this high value of  $D$ , the  $M_1$  and  $M_3$  bands move to number densities beyond our measurement range. Regions 1 and 5 thus have only the BLL bands. The region 2 (3) where the Dirac Gully band ( $M_2$ ) forms widens in range as compared to that at  $D = 0.4$  V/nm. Region 4 shows the Dirac Gully on the hole side.

The theoretically calculated  $n$  versus  $B_f$  is shown by the red solid line in Fig. S2(a-c). It was calculated from the theoretical band structures (Fig. S2(d-e)) by calculating the area of the fermi surface ( $S$ ) at constant energy and using the relation  $B_f = \hbar S / 2\pi e$ . The striking resemblance of the experimental data to the theoretical plot shows the accuracy of the measurement and sensitivity to different fermi surfaces in the band.

### S3. CALCULATION OF $\nu$ FROM LANDAU LEVEL INDEX $N$

The filling factor  $\nu$  can be expressed as a function of  $N$  as  $\nu = \alpha N + \beta$  where  $\alpha$  and  $\beta$  are constants. The following table summarizes the observed values of  $\alpha$  and  $\beta$  for the different bands in this study.

	$\alpha$	$\beta$	$\nu = \alpha N + \beta$
BLL band	4	2	6, 10, 14, 18, ...
Massive Gully	12	0	12, 24, 36, 48, ...
Massless Gully	12	6	18, 30, 42, 54, ...

TABLE S1.  $\alpha$  and  $\beta$  values corresponding to different bands.

### S4. CALCULATION OF BERRY PHASE $\Phi_B$ FROM SDH OSCILLATIONS

For a constant number density,  $n$ , and at a fixed  $T$ , the amplitude of the SdH oscillation is:

$$\Delta R_{xx} \propto \frac{\lambda}{\sinh \lambda} \cos \left( 2\pi \left( \frac{B_f}{B} + \gamma \right) \right) \quad (\text{S1})$$

The phase of oscillation is given by

$$\gamma = \frac{\Phi_B}{2\pi} - \frac{1}{2} \quad (\text{S2})$$

The oscillations will have minima at

$$2\pi \left( \frac{B_f}{B} + \gamma \right) = (2N + 1)\pi \quad N = 0, 1, 2.. \quad (\text{S3})$$

or,

$$N = B_f \left( \frac{1}{B} \right) + \left( \gamma - \frac{1}{2} \right) \quad (\text{S4})$$

The intercept of the landau level index  $N$  vs  $1/B$  plot gives  $(\gamma - 1/2)$ .

## S5. EVOLUTION OF $T_2$ AND $T_3$ GULLIES WITH DISPLACEMENT FIELD $D$

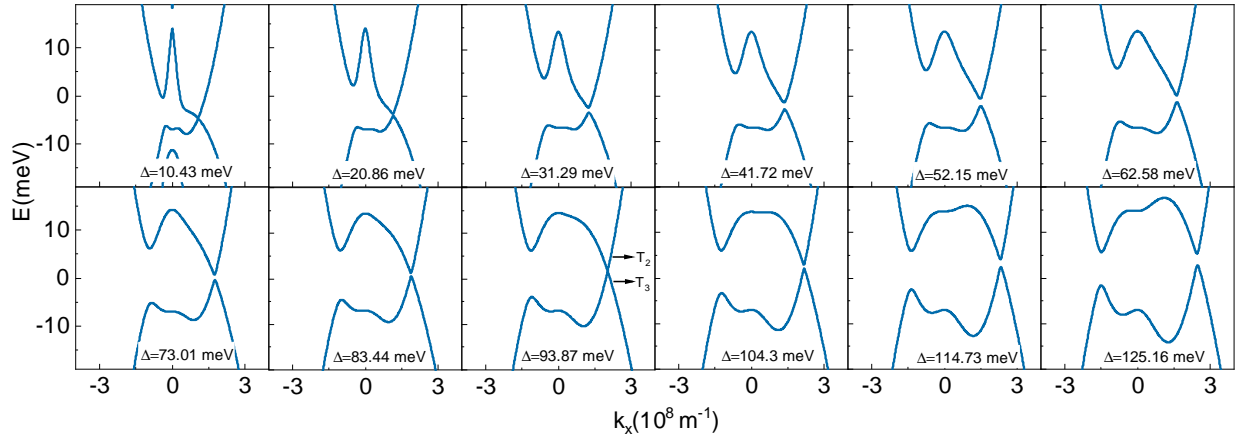


FIG. S3. **Evolution of Gully with  $D$ :** Energy  $E$  vs  $k_x$  for  $D = 0.1$  V/nm to  $D = 1.2$  V/nm. The conversion factor is  $\Delta = 104.3$  meV/Vnm.

Fig. S3 shows the evolution of the  $T_2$  and  $T_3$  gullies with the displacement field. As the displacement field  $D$  increases, the behavior of the  $T_2$  and  $T_3$  gullies becomes Dirac-like. At low  $D$ , the gully cones have a distorted parabolic shape, and as  $D$  increases, the gully cones start becoming sharp like a monolayer graphene band, which we call a Dirac band. The band gap between the  $T_2$  and  $T_3$  gullies closes at  $\Delta_c = 93.87$  meV. After  $\Delta_c$ , the band gap increases again with  $D$ . It can also be seen that with increasing  $D$ , the inter-gully distance increases.

## S6. EVOLUTION OF LANDAU LEVEL SEQUENCE AND BERRY PHASE WITH $n$ AND $D$ .

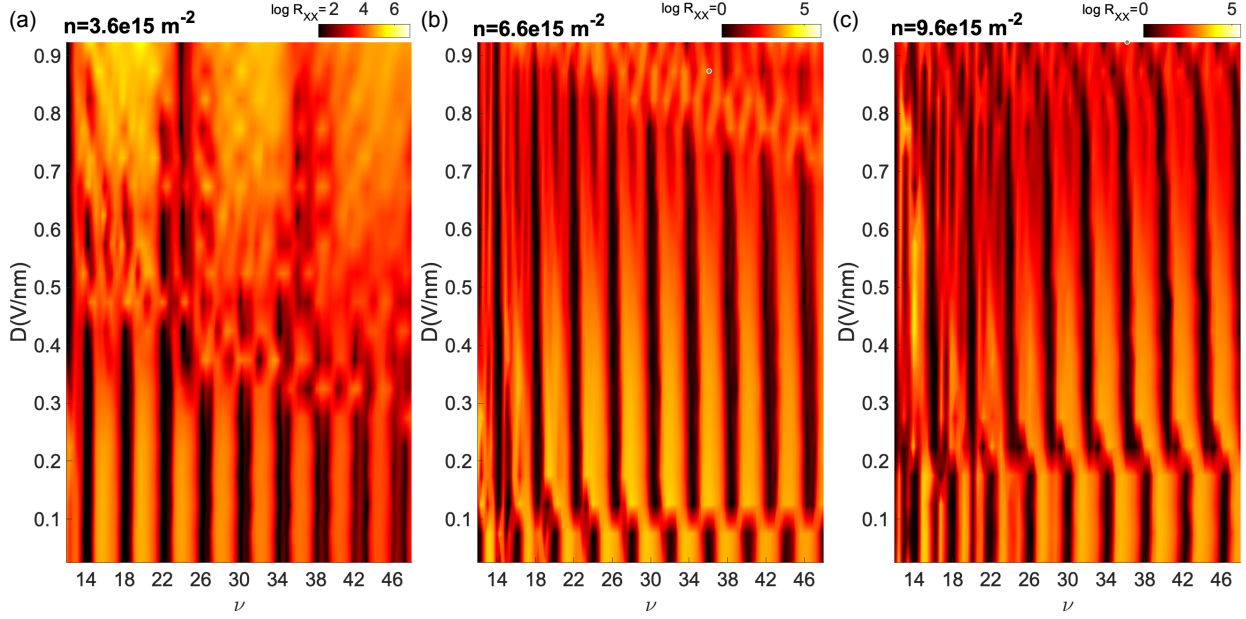


FIG. S4. **Berry Phase estimation at different  $n$ :** Contour map of  $R_{xx}$  versus  $D$  and  $\nu$  at a constant number density (a)  $n = 3.6 \times 10^{15} \text{ m}^{-2}$ . (b)  $n = 6.6 \times 10^{15} \text{ m}^{-2}$ . (c)  $n = 9.6 \times 10^{15} \text{ m}^{-2}$ .

Fig. S4(a-c) shows the contour maps of  $R_{xx}$  vs  $D$  for  $n = 3.6 \times 10^{15} \text{ m}^{-2}$ ,  $n = 6.6 \times 10^{15} \text{ m}^{-2}$  and  $n = 9.6 \times 10^{15} \text{ m}^{-2}$ . In Fig. S4(a) at low  $D$  a Landau level sequence of  $\nu = 4(N + 1/2)$  can be seen. The factor  $1/2$  arises from the underlying zeroth Landau levels of the MLL band, which results in the Berry phase of the BLL band to be  $\Phi_B = \pi$  [34]. For  $D \geq 0.5 \text{ V/nm}$ , the emergence of Landau level sequence  $\nu = 12N$  can be observed. This is due to the emergence of the three Gullies with 2-fold spin and 2-fold valley degeneracy. The Gullies in this region are massive as their Berry phase is  $2\pi$ .

In Fig. S4(b) at low  $D$  a Landau level sequence of  $\nu = 4N$  with  $\Phi_B = 2\pi$  is observed. This is because the BLL band lies in the band gap of the MLL band in this region. For  $D \geq 0.1 \text{ V/nm}$  Landau level sequence changes to  $\nu = 4(N + 1/2)$  as the BLL band now lies in the valence band of the monolayer.

In Fig. S4(c) at low  $D$ , a Landau level sequence of  $\nu = 4(N + 1/2)$  with  $\Phi_B = \pi$  is observed, which is because the BLL band lies in the conduction band of monolayer band in this region. For  $D \geq 0.2 \text{ V/nm}$ , the Landau level sequence changes to  $\nu = 4N$  as the BLL band now lies in the band



gap of the MLL band.

---

- [1] M. V. Berry, [Proceedings of the Royal Society of London. A. Mathematical and Physical Sciences](#) **392**, 45 (1984).
- [2] D. Xiao, M.-C. Chang, and Q. Niu, [Rev. Mod. Phys.](#) **82**, 1959 (2010).
- [3] G. P. Mikitik and Y. V. Sharlai, [Phys. Rev. Lett.](#) **82**, 2147 (1999).
- [4] I. A. Luk'yanchuk and Y. Kopelevich, [Phys. Rev. Lett.](#) **93**, 166402 (2004).
- [5] M. Koshino and E. McCann, [Phys. Rev. B](#) **80**, 165409 (2009).
- [6] Y. Zhang, Y.-W. Tan, H. L. Stormer, and P. Kim, [Nature](#) **438**, 201 (2005).
- [7] L. Zhang, Y. Zhang, J. Camacho, M. Khodas, and I. Zaliznyak, [Nature Physics](#) **7**, 953 (2011).
- [8] K. S. Novoselov, E. McCann, S. V. Morozov, V. I. Fal'ko, M. I. Katsnelson, U. Zeitler, D. Jiang, F. Schedin, and A. K. Geim, [Nature Physics](#) **2**, 177 (2006).
- [9] C.-H. Park and N. Marzari, [Phys. Rev. B](#) **84**, 205440 (2011).
- [10] G. P. Mikitik and Y. V. Sharlai, [Phys. Rev. B](#) **77**, 113407 (2008).
- [11] J. Li, S. Sanz, N. Merino-Díez, M. Vilas-Varela, A. Garcia-Lekue, M. Corso, D. G. de Oteyza, T. Frederiksen, D. Peña, and J. I. Pascual, [Nature Communications](#) **12**, 5538 (2021).
- [12] D. F. Liu, Q. N. Xu, E. K. Liu, J. L. Shen, C. C. Le, Y. W. Li, D. Pei, A. J. Liang, P. Dudin, T. K. Kim, C. Cacho, Y. F. Xu, Y. Sun, L. X. Yang, Z. K. Liu, C. Felser, S. S. P. Parkin, and Y. L. Chen, [Phys. Rev. B](#) **104**, 205140 (2021).
- [13] M. König, S. Wiedmann, C. Brüne, A. Roth, H. Buhmann, L. W. Molenkamp, X.-L. Qi, and S.-C. Zhang, [Science](#) **318**, 766 (2007).
- [14] P. Stepanov, Y. Barlas, S. Che, K. Myhro, G. Voigt, Z. Pi, K. Watanabe, T. Taniguchi, D. Smirnov, F. Zhang, R. K. Lake, A. H. MacDonald, and C. N. Lau, [Proceedings of the National Academy of Sciences](#) **116**, 10286 (2019).
- [15] A. Huang, S. Ke, J.-H. Guan, J. Li, and W.-K. Lou, [Phys. Rev. B](#) **109**, 045408 (2024).
- [16] P. Tiwari, S. K. Srivastav, and A. Bid, [Phys. Rev. Lett.](#) **126**, 096801 (2021).
- [17] W. Yao, S. A. Yang, and Q. Niu, [Phys. Rev. Lett.](#) **102**, 096801 (2009).
- [18] A. Varlet, D. Bischoff, P. Simonet, K. Watanabe, T. Taniguchi, T. Ihn, K. Ensslin, M. Mucha-Kruczyński, and V. I. Fal'ko, [Phys. Rev. Lett.](#) **113**, 116602 (2014).
- [19] S. Predin, P. Wenk, and J. Schliemann, [Phys. Rev. B](#) **93**, 115106 (2016).

- [20] M. Serbyn and D. A. Abanin, [Phys. Rev. B](#) **87**, 115422 (2013).
- [21] P. Rao and M. Serbyn, [Phys. Rev. B](#) **101**, 245411 (2020).
- [22] T. Morimoto and M. Koshino, [Phys. Rev. B](#) **87**, 085424 (2013).
- [23] R. de Gail, M. O. Goerbig, and G. Montambaux, [Phys. Rev. B](#) **86**, 045407 (2012).
- [24] A. Varlet, M. Mucha-Kruczyński, D. Bischoff, P. Simonet, T. Taniguchi, K. Watanabe, V. Fal'ko, T. Ihn, and K. Ensslin, [Synthetic Metals](#) **210**, 19 (2015), reviews of Current Advances in Graphene Science and Technology.
- [25] A. M. Seiler, F. R. Geisenhof, F. Winterer, K. Watanabe, T. Taniguchi, T. Xu, F. Zhang, and R. T. Weitz, [Nature](#) **608**, 298 (2022).
- [26] G.-Q. Qin, F.-M. Jing, T.-Y. Hao, S.-L. Jiang, Z.-Z. Zhang, G. Cao, X.-X. Song, and G.-P. Guo, [Phys. Rev. Lett.](#) **134**, 036301 (2025).
- [27] A. A. Zibrov, P. Rao, C. Kometter, E. M. Spanton, J. I. A. Li, C. R. Dean, T. Taniguchi, K. Watanabe, M. Serbyn, and A. F. Young, [Phys. Rev. Lett.](#) **121**, 167601 (2018).
- [28] H. Zhou, N. Auerbach, M. Uzan, Y. Zhou, N. Banu, W. Zhi, M. E. Huber, K. Watanabe, T. Taniguchi, Y. Myasoedov, B. Yan, and E. Zeldov, [Nature](#) **624**, 275 (2023).
- [29] S. K. Srivastav, A. Udupa, K. Watanabe, T. Taniguchi, D. Sen, and A. Das, [Phys. Rev. Lett.](#) **132**, 096301 (2024).
- [30] P. Tiwari, M. K. Jat, A. Udupa, D. S. Narang, K. Watanabe, T. Taniguchi, D. Sen, and A. Bid, [npj 2D Materials and Applications](#) **6**, 68 (2022).
- [31] S. Kaur, T. Chanda, K. R. Amin, D. Sahani, K. Watanabe, T. Taniguchi, U. Ghorai, Y. Gefen, G. J. Sreejith, and A. Bid, [Nature Communications](#) **15**, 8535 (2024).
- [32] C. Küppersbusch and L. Fritz, [Phys. Rev. B](#) **96**, 205410 (2017).
- [33] K. S. Novoselov, A. K. Geim, S. V. Morozov, D. Jiang, M. I. Katsnelson, I. V. Grigorieva, S. V. Dubonos, and A. A. Firsov, [Nature](#) **438**, 197 (2005).
- [34] B. Datta, P. C. Adak, L. kun Shi, K. Watanabe, T. Taniguchi, J. C. W. Song, and M. M. Deshmukh, [Science Advances](#) **5**, eaax6550 (2019).
- [35] M. S. Dresselhaus and G. Dresselhaus, [Advances in Physics](#) **51**, 1 (2002).
- [36] J. C. Slonczewski and P. R. Weiss, [Phys. Rev.](#) **109**, 272 (1958).
- [37] J. McClure, [Carbon](#) **7**, 425 (1969).
- [38] C. Cong, T. Yu, K. Sato, J. Shang, R. Saito, G. F. Dresselhaus, and M. S. Dresselhaus, [ACS Nano](#) **5**, 8760 (2011).

- [39] T. A. Nguyen, J.-U. Lee, D. Yoon, and H. Cheong, [Scientific Reports](#) **4**, 4630 (2014).
- [40] A. Venugopal, J. Chan, X. Li, C. W. Magnuson, W. P. Kirk, L. Colombo, R. S. Ruoff, and E. M. Vogel, [Journal of Applied Physics](#) **109**, 104511 (2011).